Nanoscale

PAPER

View Article Online
View Journal

Cite this: DOI: 10.1039/d6nr00390g

Templated growth of perovskite shells on single-walled carbon nanotubes: a solution-processable route towards tailored devices

Gririraj Manoharan, Xuan Li, Stoichko Dimitrov * and Matteo Palma *

Carbon nanotube (CNT)-based nanohybrids have shown considerable potential for the construction of functional heterostructures with a diverse range of optoelectronic properties. To fully exploit their potential, high-performance solution-processed semiconductors with precisely controlled optical and electronic characteristics are desirable. In this regard, halide perovskite semiconductors are known for their excellent and tunable optoelectronic properties and hence are ideal candidates for integration into CNT-based nanohybrids towards the construction of systems and devices with enhanced functionality. Here we present a strategy for the synthesis of solution-processable nanohybrids made of single-walled carbon nanotubes (SWCNTs) and perovskite semiconductors, using methylammonium lead iodide ($MAPbI_3$) and cesium lead iodide ($CsPbI_3$), as proof-of-concept systems: the CNTs act as templates for the facile and tunable formation of perovskite nanocrystals. We investigated the structural and electronic properties of the assembled SWCNT heterostructures and demonstrated their integration (from solution) into field-effect transistor device configurations. By harnessing the synergistic properties of carbon nanotubes and perovskites, we discuss pathways for the development of photoresponsive devices employing these nanohybrids. The facile, solution-processable methodology we developed enables the spatial positioning of SWCNT–perovskite intermediate nanohybrids prior to crystallization, allowing the integration of nanoscale SWCNT bundles into FET architectures toward optoelectronic applications.

Received 28th January 2026,
Accepted 11th April 2026

DOI: 10.1039/d6nr00390g

rsc.li/nanoscale

Introduction

The ability to combine the structural and optoelectronic properties of different nanomaterials into novel heterostructures with enhanced functionality is of great interest, in particular for optoelectronic applications.[1–3] In this context, carbon nanotube (CNT)-based nanohybrids have drawn attention due to the one-dimensional (1D) charge transport character of the nanotubes, their high surface area, and the resulting ability to facilitate charge transfer at heterointerfaces for the generation of low-dimensional heterostructures with tunable electronic, optical, and mechanical properties.[1,3–9] Of particular interest is the integration of CNTs with materials that possess tunable optical and electronic properties.[1–3,10,11] Among these, perovskite semiconductors have shown great potential since the first reports of high-performance perovskite solar cells in 2012.[12–15] They have the general formula ABX_3 (where A = $CH_3NH_3^+$ [methylammonium (MA)], $CH(NH_2)_2^+$ [formamidinium (FA)], or Cs^+; B = Pb^{2+} or Sn^{2+}; and X = I^-, Br^-, or Cl^-) and have found different optoelectronics applications, including the use in field-effect transistors,[16,17] light-emitting diodes (LEDs),[18,19] photodetectors,[20,21] solar cells[22] and gas sensors.[23] Advantages of perovskites are their solution processability and lightweight nature, which can simplify device fabrication without sacrificing performance. Furthermore, perovskite semiconductors are multi-crystalline and exhibit high light absorption coefficients, tunable band gaps, high photoluminescence quantum yields, and long carrier diffusion lengths, making them highly attractive for integration into hybrid nanostructures.[24–27]

In this regard, the integration of multi-walled (MW) and single-walled (SW) CNTs with perovskites has been investigated primarily as thin films or dopants, demonstrating the potential of these heterostructures for optoelectronic applications.[22,28–36] The synergy between perovskites and carbon nanotubes has recently paved the way for highly sensitive, flexible and stable next-generation neuromorphic sensor arrays and advanced photodetectors.[37–42] For instance, SWCNTs were spray-coated as aligned arrays, followed by the spin-coating of metal halide perovskite thin films onto pre-patterned substrates, to facilitate the demonstration of optical

Department of Chemistry, Queen Mary University of London, London E1 4NS, UK.
E-mail: s.dimitrov@qmul.ac.uk, m.palma@qmul.ac.uk

switching behavior.[43] More recently, Wang *et al.* reported a growth strategy on SWCNT thin films, achieving high performance through optimized interface engineering with ligand-coated perovskite quantum dots.[29] Growing perovskite nanocrystals inside CNTs has also been established *via* melt insertion and gas/liquid-phase infiltration, yielding an atomically resolved interface structure for ultra-low power transistors and X-ray detectors.[44–47] However, only a limited number of studies have demonstrated the growth of perovskite nanocrystals directly on the surface of the CNTs and have done this by employing MWCNTs,[4,28,48] which have limited utility as transistor channels.[49] Notably, Lee *et al.* demonstrated a nanoseeding strategy to grow perovskite nanocrystals on MWCNTs, which were subsequently employed as green-emitting nanohybrids for UV detection and anticounterfeiting QR codes.[28]

In this study, we developed a strategy to grow perovskite nanocrystals as shells on SWCNTs and fabricated photoresponsive devices comprising CNT–perovskite nanohybrids. This strategy offers unique flexibility, enabling the growth of nanohybrids under annealing conditions, and can be potentially tailored to specific device configurations. We demonstrated the general applicability of our strategy employing semiconducting SWCNTs of two distinct chiralities, namely, (7,6) and (6,5), and two different perovskite materials, namely, methylammonium lead iodide ($MAPbI_3$) and cesium lead iodide ($CsPbI_3$). The coupling between the two nanomaterials in the hybrid was investigated *via* structural and spectroscopic characterization. As a proof of concept, solution-processable photo-responsive devices with high responsivity and detectivity were fabricated and characterized. Our method for synthesizing SWCNT–perovskite nanohybrids enables the construction of nanomaterials with direct and continuous hetero-interfaces, for potential applications in optoelectronics, sensing and communication.[4,50–52]

Results and discussion

Hybrid SWCNT–perovskite structures were prepared from solution for four hybrid combinations, using SWCNTs with (7,6) and (6,5) enriched chiralities (see Fig. S1) as templates to grow two types of perovskites: methylammonium lead iodide ($MAPbI_3$) and cesium lead iodide ($CsPbI_3$). A three-step perovskite crystallisation approach was developed for their synthesis [details of the methodology are presented in the Experimental section]. In the first step, perovskite precursors were mixed with SWCNTs in dimethylformamide (DMF). Ethyl acetate (EA) antisolvent was then introduced into the solution to facilitate perovskite nucleation.[48,53] In the third step, the solutions were deposited onto surfaces and annealed to induce perovskite crystal growth on the SWCNT nanotube bundles. The step-by-step synthetic approach including a representative scanning electron microscopy (SEM) image of a SWCNT–perovskite nanohybrid device is shown in Fig. 1a. The morphology and uniformity of the SWCNT–perovskite nanohybrids were first examined using transmission and scanning electron microscopy (TEM and SEM); the results are shown in Fig. 1b, c and Fig. S2a–f.

SEM and TEM imaging revealed nanocrystals on the surfaces of the SWCNTs, with growth occurring selectively on the nanotube surfaces and independently of SWCNT chirality. The average height distribution of the nanohybrids was found to be 26.3 nm with a standard deviation (SD) of 8.6 nm, highlighting the formation of bundles of SWCNT–perovskite nanohybrids (see Fig. S3 for AFM images of a typical SWCNT–perovskite nanohybrid bundle and its corresponding height profile). SEM images further confirmed the specificity of the growth, demonstrating dense crystal formation without significant pinholes, as highlighted in Fig. 1b and c [see Fig. S2a–f for TEM images of perovskite nanohybrid bundles with (7,6), (6,5) and mixed chirality short (ss) SWCNTs, and Fig. S4 for HRTEM images with the corresponding EDS mapping and spectra].

Fig. 2 presents the X-ray diffraction (XRD) patterns of the nanohybrids containing (7,6) and (6,5) nanotubes, compared to those of $MAPbI_3$ and $CsPbI_3$ films. This analysis substantiates the growth of $MAPbI_3$ nanocrystals (Fig. 2a) on the SWCNTs, with distinctive peaks observed at 14.1°, 28.5°, 32.0°, and 40.6°, corresponding to the (110), (220), (310), and (224) planes of the orthorhombic perovskite crystal structure.[54] Fig. 2b shows the characteristic diffraction peaks of $CsPbI_3$ nanocrystals grown on (7,6) and (6,5) at 10°, 13.11°, 22.6°, 26.47°, 31.39° and 37.66°, assigned to the (020), (012), (112), (110), (016), and (110) planes of the orthorhombic γ-phase.[55–57] The comparatively low intensity of these peaks for SWCNT-perovskite hybrids, relative to those of pure perovskite thin films, can be due to the formation of bundles on the substrate surface, making it less dense. X-ray photoelectron spectroscopy (XPS) analysis of Pb 4f and I 3d for both $MAPbI_3$ and $CsPbI_3$ (Fig. S5 and S6) revealed a small shift in the binding energy likely related to electronic interactions between SWCNTs and $MAPbI_3$ perovskite crystals, as previously shown in similar systems.[4]

Raman spectroscopy investigations provided insight into the electronic interactions between the perovskites and the (7,6) and (6,5) SWCNTs. In the pristine SWCNTs, the G and G′ bands were located at 1594 cm^{-1} and 2602.7 cm^{-1} for the (7,6) chirality, and at 1590 cm^{-1} and 2592.5 cm^{-1} for the (6,5) chirality, consistent with literature values.[58] A blue shift in the G′ band was identified for all SWCNT–perovskite nanohybrids, with peak values recorded at 2701.2 cm^{-1} for (7,6) $MAPbI_3$, 2710.99 cm^{-1} for (7,6) $CsPbI_3$, 2690.5 cm^{-1} for (6,5) $MAPbI_3$, and 2692.14 cm^{-1} for (6,5) $CsPbI_3$, respectively. This shift has been previously assigned to a decreased electron density in the SWCNT π-network, suggesting net hole transfer from the perovskite nanocrystals to the SWCNTs; lattice-induced strain from the perovskite shell growth might also contribute to the observed shifts (Fig. 3).[32,43,59–61]

Photoluminescence (PL) spectroscopy characterization of our SWCNT–perovskite hybrids detected emission from the perovskite crystals. While neat perovskite films displayed PL peaks at 780 nm for $MAPbI_3$ and 700 nm for $CsPbI_3$, the CNT–

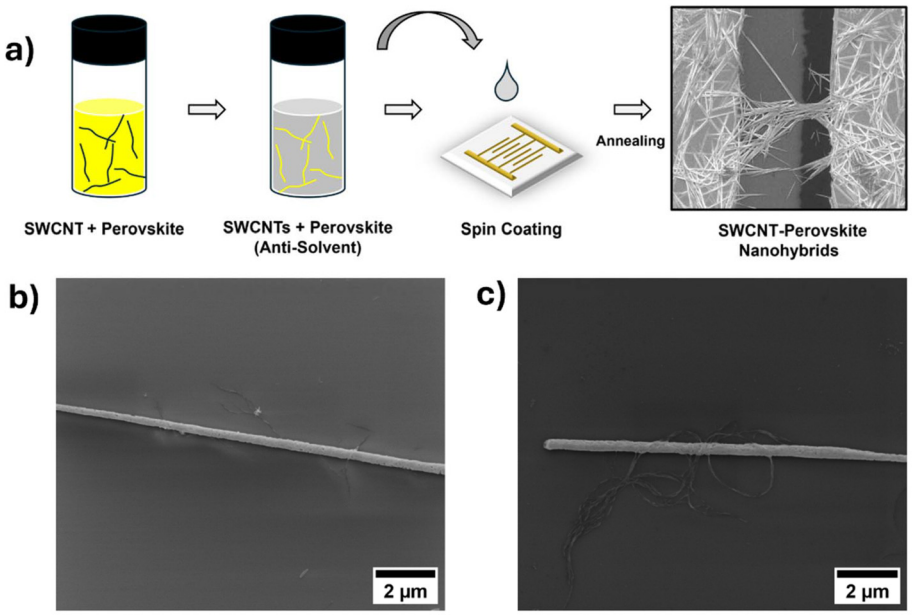

Fig. 1 (a) Schematic of the step-by-step procedure for the growth of perovskite nanocrystals ($MAPbI_3$ and $CsPbI_3$) on single-walled carbon nanotubes and a representative SEM image of the device. SEM images of the resulting nanohybrids: (b) (7,6) SWCNT–$MAPbI_3$ and (c) (6,5) SWCNT–$MAPbI_3$.

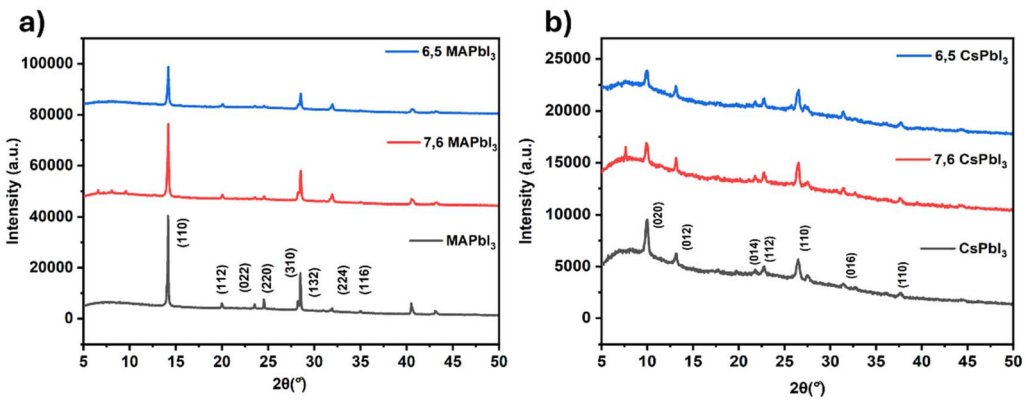

Fig. 2 XRD patterns of (7,6) and (6,5) SWCNT–perovskite nanohybrids: (a) SWCNT–$MAPbI_3$ and (b) SWCNT–$CsPbI_3$, with neat $MAPbI_3$ and $CsPbI_3$ films, respectively.

perovskite nanohybrids exhibited a small blue shift for both types of perovskites in the nanohybrids (Fig. 4a and b). This shift is potentially attributable to the Burstein–Moss effect[4] and is consistent with the energy shifts observed in XPS and Raman caused by charge transfer from perovskite nanocrystals to carbon nanotubes. The broadening of the $MAPbI_3$ PL spectra in the two nanohybrids can be caused by variations in defect properties and interaction-induced strain, as the perovskite crystallites are grown on the SWCNT seeds. The XRD results in Fig. 2 do not show any changes in the bulk crystal lattice for this sample, suggesting that surface defects are responsible for the observed spectral changes. We further characterized mixed-chirality (ss) SWCNT–perovskite nanohybrids, and they also exhibited the same PL characteristics (Fig. S7). Moreover, we observed quenching of the PL emission of the nanotubes upon formation of perovskite nanohybrids (Fig. S8), strongly indicating electronic coupling between the CNTs and the perovskites.

The electronic coupling in the nanohybrids was further corroborated and quantified *via* time-resolved PL spectroscopy characterisation, employed to assess the decay dynamics of the electronic excitation in (7,6) SWCNT–$MAPbI_3$ (Fig. 4c). The samples were excited with a 635 nm laser diode, and PL was detected at the perovskite emission maximum at 778 nm. The PL decay of $MAPbI_3$ was nearly mono-exponential, while the hybrids displayed a clear bi-exponential decay. The PL lifetime was found to decrease from 3.8 ns for $MAPbI_3$ to 0.7 ns in the SWCNT–$MAPbI_3$ nanohybrids. This indicates strong quench-

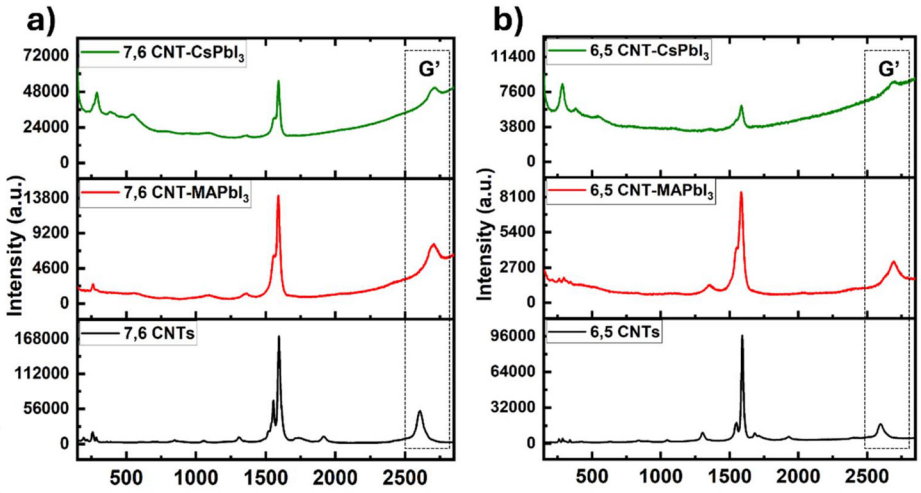

Fig. 3 Raman spectra of (a) (7,6) SWCNT-based and (b) (6,5) SWCNT-based pristine nanotubes and nanotube–perovskite nanohybrids ($MAPbI_3$ and $CsPbI_3$).

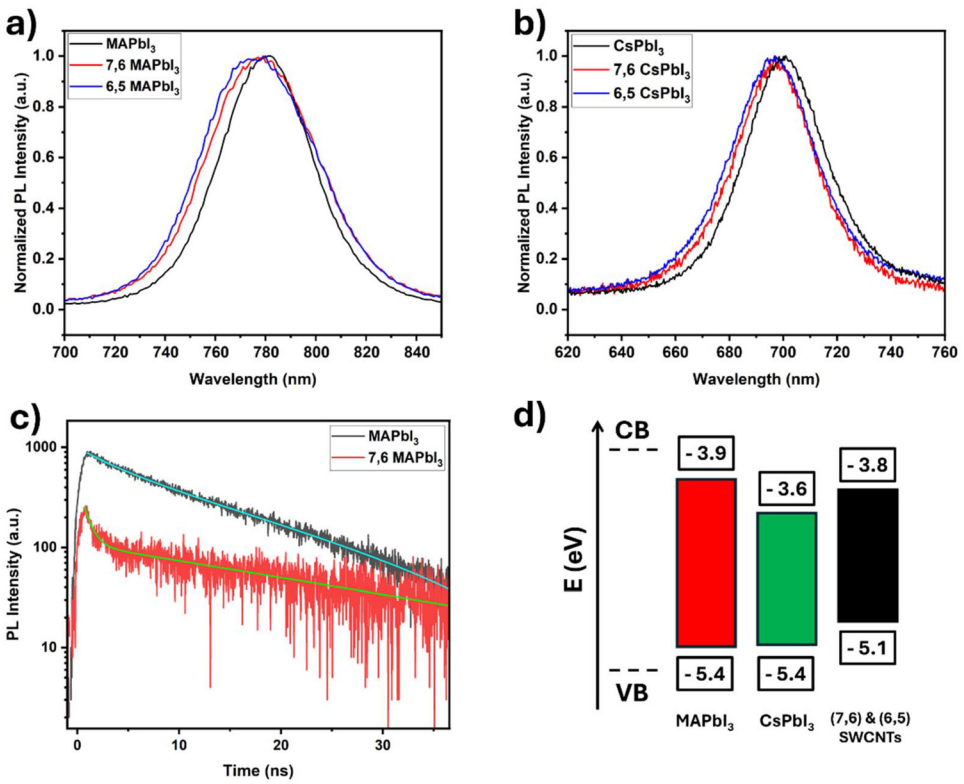

Fig. 4 Steady-state photoluminescence spectra of perovskite films: (a) $MAPbI_3$ and (b) $CsPbI_3$, and their perovskite nanohybrids with (7,6) and (6,5) SWCNTs, acquired with 405 nm excitation. (c) Time-resolved photoluminescence of $MAPbI_3$ and (7,6) SWCNT–$MAPbI_3$ nanohybrids using 635 nm laser illumination. (d) Schematic illustration of the energy band diagram of $MAPbI_3$, $CsPbI_3$ and (7,6) & (6,5) SWCNTs.

ing of photoexcited charges, most likely due to charge transfer between the SWCNTs and the perovskite crystals. The electronic structures of the perovskites and the SWCNTs[62–65] suggest that the dominant charge transfer process can be ascribed to hole transfer from the perovskite to the nanotubes (see Fig. 4d), revealing close electronic coupling between the two nanostructures. The photoinduced charge transfer processes observed in the SWCNT–perovskite nanohybrids make these heterostructures promising for optoelectronic applications.[33,35,66]

In this regard, we fabricated phototransistor devices by spin-coating the SWCNT–perovskite intermediate nanohybrid solutions onto gold-plated interdigitated electrodes, exhibiting a gap of 3 μm, patterned on Si/SiO_2 substrates (see the SI). Field-effect transistor (FET) devices exhibited typical p-type behaviour, as expected for pristine semiconducting SWCNTs (Fig. S9). Post annealing, the SWCNT–perovskite devices were illuminated for 10 s at 20 s intervals using consecutively laser diodes with wavelengths of 650 nm, 532 nm, and 405 nm. Photocurrent was measured (in a vacuum) through the source (S) and drain (D) electrodes with a constant S–D bias (V_{DS}) of 1 V. All (7,6), (6,5) and (ss) SWCNT–perovskite nanohybrids exhibited a positive photocurrent change upon illumination at all three wavelengths (Fig. 5a–d, S10a and S10b), while the pristine SWCNTs exhibited the aforementioned decrease at 405 nm and minimal response at 532 nm and 650 nm illumination (Fig. 5c, f and S7c). The behaviour of our SWCNT–perovskite nanohybrids is consistent with photoinduced hole transfer from the perovskite nanocrystals to nanotubes, in accordance with the PL data and band alignment rationalisation discussed above (Fig. 4). Stability tests performed on a SWCNT–$MAPbI_3$ photoresponsive device stored in air for one week showed consistent performance, while reproducibility tests on multiple devices fabricated from different batches exhibited similar photoresponse characteristics (Fig. S11 and S12). In order to quantify the photodetector performance, we determined the photoresponsivity (R) and specific detectivity (D^*) of all our SWCNT–perovskite devices under 405 nm, 532 nm and 650 nm light illumination (Fig. 5g, h and Tables S13, S14). We observed the highest photoresponsivity and detectivity values under 650 nm illumination. In particular, the responsivity values at 650 nm for the SWCNT–$MAPbI_3$ nanohybrids were found to be 8.42×10^3 A W^{-1} and 1.71×10^4 A W^{-1}, for (7,6) and (6,5) $MAPbI_3$, respectively, while we measured responsivity values of 2.30×10^4 A W^{-1} and 2.53×10^4 A W^{-1} for (7,6) and (6,5) $CsPbI_3$ nanohybrids, respectively. The highest detectivity (D^*) was found to be 6.02×10^{12} Jones for (7,6) $MAPbI_3$ and 1×10^{13} Jones for (6,5) $MAPbI_3$ at 650 nm, while $CsPbI_3$ nanohybrid detectivity was determined to be 1.09×10^{13} Jones for (7,6) $CsPbI_3$ and 1.12×10^{13} Jones for (6,5) $CsPbI_3$ at 650 nm.

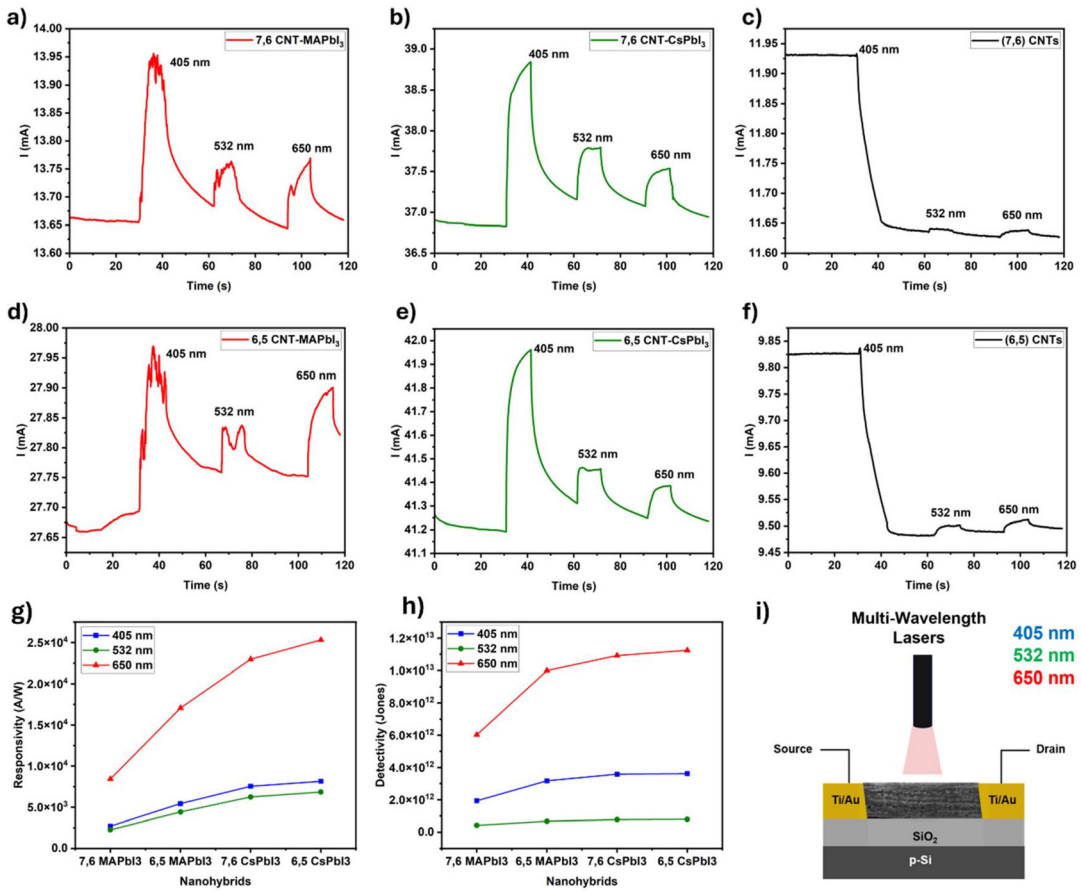

Fig. 5 Photoresponse of SWCNT devices and SWCNT–perovskite nanohybrids upon laser illumination with 405 nm, 532 nm and 650 nm wavelengths: (a) (7,6) CNT–$MAPbI_3$, (b) (7,6) CNT–$CsPbI_3$, (c) pristine (7,6) SWCNTs, (d) (6,5) CNT–$MAPbI_3$, (e) (6,5) CNT–$CsPbI_3$, and (f) pristine (6,5) SWCNTs. (g) Photoresponsivity (R) and (h) detectivity (D^*) of the (7,6) and (6,5) carbon nanotube–perovskite nanohybrids at three different wavelengths (405 nm, 532 nm and 650 nm; uncorrected for photon intensity). (i) Cartoon of photoresponse characterization of an SWCNT–perovskite nanohybrid FET device.

Previous reports on CNT–perovskite photodetectors, primarily based on thin-film architectures, have demonstrated admirable performance at shorter wavelengths, with responsivities in the range of 1.6×10^6 A W^{-1}–1.65×10^7 A W^{-1} and detectivities reaching 3.1×10^{15} Jones–2×10^{16} Jones at 405 nm, and up to 6.3×10^4 A W^{-1} and 1.12×10^{17} Jones at 532 nm.[29,37] In comparison, our devices comprising limited individual SWCNT–perovskite nanohybrid bundles (~26.3 nm) exhibited responsivities of 3.74×10^3–7.02×10^3 A W^{-1} and detectivities of 1.44×10^{12}–3.31×10^{12} Jones at 405 nm, and responsivities of 4.65×10^3–1.08×10^4 A W^{-1} with detectivities of 2.79×10^{12}–5.90×10^{12} Jones at 532 nm. While these values are modest relative to those of the best-performing thin-film systems, they are among the highest reported for nanoscale, bundle-based SWCNT–perovskite architectures. Notably, at 650 nm, where literature performance is limited,[38] our devices achieved superior responsivities of up to 2.53×10^4 A W^{-1} and detectivities of up to 1.12×10^{13} Jones. These findings highlight the potential of our nanohybrid bundle design for efficient broadband photodetection, particularly in the red spectral region.[29,35,37–42]

Conclusions

In summary, we presented a facile solution-processable strategy for the growth of perovskite nanocrystals as shells on SWCNTs. (7,6), (6,5) and mixed-chirality short (ss) SWCNTs were employed as templates for the synthesis of two types of perovskites ($MAPbI_3$ and $CsPbI_3$), resulting in the formation of SWCNT–perovskite nanohybrids. XRD and PL spectroscopy characterization confirmed the formation of perovskites, while SEM and TEM showed uniform and dense perovskite coverage on SWCNT bundles. Electronic interactions between the perovskites and SWCNTs were detected by XPS and Raman spectroscopy, while steady-state and time-resolved PL experiments allowed us to cast light on the photoinduced charge transfer processes among the hybrid components. Moreover, we fabricated solution-processable SWCNT–perovskite FET devices; these exhibited photocurrent responses consistent with a hole transfer process from the perovskite to the SWCNTs, corroborating the aforementioned PL spectroscopy investigations. Finally, high responsivity and detectivity values were achieved in our nanohybrid devices, broadly in line with most of the previously presented perovskite–CNT thin-film photodetectors. Notably, we achieved selective growth of perovskite nanocrystals on SWCNTs and fabricated devices employing only a limited number of hybrid bundles bridging prepatterned electrodes. Our approach for the direct growth of perovskite nanocrystals on SWCNTs is of general applicability, and the solution-processable strategy allows spatial positioning of SWCNT–perovskite intermediate nanohybrids prior to crystallization, enabling tuning of the annealing process and integration of nanoscale SWCNT bundles into the device configuration. This can pave the way for the development of future perovskite nanohybrid structures to be employed in various device architectures for diverse optoelectronic applications. SWCNTs have smaller sizes and, most importantly, chirality-dependent optoelectronic properties,[67] making them compatible with the requirements of computing and electronic devices.[68–70] Integrating SWCNTs can offer various advantages for the formation of SWCNT–perovskite nanohybrids with enhanced functionality in optoelectronic applications.[43,71]

Experimental section

Materials preparation and device fabrication

Materials. Single-walled carbon nanotubes (SWCNTs) with chiralities including (7,6) (77% carbon nanotubes) and (6,5) (95% carbon nanotubes) were purchased from Sigma-Aldrich. Short (ss) mixed-chirality SWCNTs (90% carbon nanotubes) were purchased from US Research Nanomaterials, Inc., *N*,*N* dimethylformamide (DMF, 99.8% anhydrous), ethyl acetate (EA), methyl ammonium iodide (CH_3NH_3I), cesium iodide (CsI) and lead iodide (PbI_2) were all purchased from Sigma-Aldrich and used as received.

Dispersion of SWCNTs. 0.5 mg of SWCNTs with chiralities including (7,6), (6,5), and short (ss) mixed-chirality nanotubes were separately dispersed in 1 mL of DMF through ultrasonication (Branson 2800, 130 W). The dispersion process of these three batches was carried out for 2 hours to ensure effective separation of nanotubes. Following ultrasonication, the mixture was centrifuged at 10 000 rpm for 5 minutes to obtain a uniformly dispersed SWCNT suspension which was suitable for further processing and integration with perovskite materials.

Preparation of perovskite precursors. The three-step nanotube–perovskite crystallization process begins by combining the SWCNT solution with perovskite precursors. For $MAPbI_3$, 0.17 g of methylammonium iodide (CH_3NH_3I) and 0.46 g of lead iodide (PbI_2) were dissolved in 1 mL of DMF and stirred overnight at 60 °C under a controlled atmosphere within a glovebox. Similarly, for $CsPbI_3$, 0.25 g of cesium iodide (CsI) and 0.46 g of lead iodide (PbI_2) were dissolved in 1 mL of DMF and stirred overnight at 100 °C under the same glovebox conditions. After stirring, both precursor solutions, prepared at a concentration of 1 M, were filtered through a 0.45 μm pore polytetrafluoroethylene (PTFE) filter to remove undissolved particles, ensuring their suitability for integration with SWCNTs.

Mixing of perovskite precursors with SWCNTs. The prepared perovskite precursor solution (50 μL) was mixed with the SWCNT dispersion (950 μL) *via* ultrasonication (130 W) for 1 hour. This step was performed to facilitate the uniform distribution of perovskite precursors on the SWCNT surface, ensuring effective interaction between the two materials. Subsequently, 100 μL of the perovskite–SWCNT mixture was added to 1 mL of ethyl acetate, an anti-solvent, and sonicated for an additional hour. This anti-solvent approach creates favourable nucleation sites for the perovskite to grow around the SWCNTs, forming well-defined nanohybrids.

Device fabrication. The resulting mixture was spin-coated onto various substrates, including pre-patterned interdigitated gold electrodes (electrode gap size: 3 μm; X&X Technology, UK), glass substrates, and indium tin oxide (ITO) substrates, for subsequent characterization. Spin coating was carried out for 30 seconds at 3000 rpm for homogeneous distribution of the mixture on the substrate surface. After deposition, the film substrates were annealed at different temperatures (100 °C for $MAPbI_3$ and 200 °C for $CsPbI_3$ for 30 minutes, respectively) to facilitate crystallization and improve the structural integrity of the nanohybrids. The annealing process also helps in optimizing the electronic and optoelectronic properties of the films by enhancing the interaction between the SWCNTs and perovskite nanocrystals.

Electrical measurements. Electrical measurements were performed using a probe station (PS-100, Lakeshore) equipped with a semiconducting parameter analyser (Keithley, 4200SCS) at room temperature. The analyser recorded the current through the devices (I_{DS}) where a constant voltage (1 V) was applied to the source and drain electrodes. After the current stabilized, lasers of different wavelengths, typically, 405 nm, 532 nm and 650 nm, were illuminated onto the devices one after the other at regular time intervals (10 s ON time). We repeated this process to test the reproducibility of the devices. Gate dependence characterization of the devices was carried out by measuring I_{DS} *vs.* V_G curves in the range of −10 to 10 V at a fixed V_{DS} of 1 V, using an HP 4148B semiconductor parameter analyzer.

Responsivity (R) and detectivity (D^*). We calculated the responsivity (R) and detectivity (D^*) of our devices, which are two essential parameters employed to evaluate photodetection devices. Responsivity can be obtained using $R = (I_{light} - I_{dark})/(S \times P)$, where I_{light} is the current under illumination, I_{dark} is the current under darkness, S is the effective area and P is the power density of the light source. The specific detectivity can be calculated using $D^* = RS1/2/(2qI_{dark})1/2$, where R is the responsivity, S is the effective area, and q is the electron charge. The effective area of the device (S) is determined using the formula: S = (total area) − (non-active area). Here, the total area refers to the entire region between the device electrodes, while the non-active area represents the portion where no carbon nanotube–perovskite nanohybrids are present between the electrodes.

Conflicts of interest

There are no conflicts to declare.

Data availability

Supplementary information (SI): additional experimental data. See DOI: https://doi.org/10.1039/d6nr00390g.

Acknowledgements

We thank Dr Suresh Maniarasu, Helmholtz-Zentrum Berlin, Germany, for assisting with XPS analysis. We thank Dr Thibault Degousse and Dr Teymour Talha-Dean for their valuable inputs. This work was partly funded by EP/V010913/1.

References

1 C. Allard, L. Alvarez, J.-L. Bantignies, N. Bendiab, S. Cambré, S. Campidelli, J. A. Fagan, E. Flahaut, B. Flavel, F. Fossard, E. Gaufrès, S. Heeg, J.-S. Lauret, A. Loiseau, J.-B. Marceau, R. Martel, L. Marty, T. Pichler, C. Voisin, S. Reich, A. Setaro, L. Shi and W. Wenseleers, *Chem. Soc. Rev.*, 2024, **53**, 8457–8512.
2 D. Eder, *Chem. Rev.*, 2010, **110**, 1348–1385.
3 R. Xiang, T. Inoue, Y. Zheng, A. Kumamoto, Y. Qian, Y. Sato, M. Liu, D. Tang, D. Gokhale, J. Guo, K. Hisama, S. Yotsumoto, T. Ogamoto, H. Arai, Y. Kobayashi, H. Zhang, B. Hou, A. Anisimov, M. Maruyama, Y. Miyata, S. Okada, S. Chiashi, Y. Li, J. Kong, E. I. Kauppinen, Y. Ikuhara, K. Suenaga and S. Maruyama, *Science*, 2020, **367**, 537–542.
4 M. Shu, Z. Zhang, Z. Dong and J. Xu, *Carbon*, 2021, **182**, 454–462.
5 Q. Ye, X. Xu, A. Paghi, T. Bamford, B. R. Horrocks, A. Houlton, G. Barillaro, S. Dimitrov and M. Palma, *Adv. Funct. Mater.*, 2021, **31**, 2105719.
6 N. Roy, M. S. Ahmed, H. K. Lee and S. Jeon, *Nanoscale*, 2024, **16**, 7532–7546.
7 M. Freeley, A. Attanzio, A. Cecconello, G. Amoroso, P. Clement, G. Fernandez, F. Gesuele and M. Palma, *Adv. Sci.*, 2018, **5**, 1800596.
8 A. Vasylenko, S. Marks, J. M. Wynn, P. V. C. Medeiros, Q. M. Ramasse, A. J. Morris, J. Sloan and D. Quigley, *ACS Nano*, 2018, **12**, 6023–6031.
9 P. Clément, X. Xu, C. T. Stoppiello, G. A. Rance, A. Attanzio, J. N. O'Shea, R. H. Temperton, A. N. Khlobystov, K. R. J. Lovelock, J. M. Seymour, R. M. Fogarty, A. Baker, R. A. Bourne, B. Hall, T. W. Chamberlain and M. Palma, *Angew. Chem., Int. Ed.*, 2019, **58**, 9928–9932.
10 C. J. Shearer, A. Cherevan and D. Eder, *Adv. Mater.*, 2014, **26**, 2295–2318.
11 N. Sultana, H. M. Dewey, A. G. Arellano and J. Budhathoki-Uprety, *Chem. Mater.*, 2024, **36**, 4034–4053.
12 M. M. Lee, J. Teuscher, T. Miyasaka, T. N. Murakami and H. J. Snaith, *Science*, 2012, **338**, 643–647.
13 H.-S. Kim, C.-R. Lee, J.-H. Im, K.-B. Lee, T. Moehl, A. Marchioro, S.-J. Moon, R. Humphry-Baker, J.-H. Yum, J. E. Moser, M. Grätzel and N.-G. Park, *Sci. Rep.*, 2012, **2**, 591.
14 M. A. Green and A. Ho-Baillie, *ACS Energy Lett.*, 2017, **2**, 822–830.
15 N.-G. Park, *Mater. Today*, 2015, **18**, 65–72.
16 M. Spina, B. Náfrádi, H. M. Tóháti, K. Kamarás, E. Bonvin, R. Gaal, L. Forró and E. Horváth, *Nanoscale*, 2016, **8**, 4888–4893.
17 T. Wu, W. Pisula, M. Y. A. Rashid and P. Gao, *Adv. Electron. Mater.*, 2019, **5**, 1900444.

18 Z.-K. Tan, R. S. Moghaddam, M. L. Lai, P. Docampo, R. Higler, F. Deschler, M. Price, A. Sadhanala, L. M. Pazos, D. Credgington, F. Hanusch, T. Bein, H. J. Snaith and R. H. Friend, *Nat. Nanotechnol.*, 2014, **9**, 687–692.
19 J. Wang, N. Wang, Y. Jin, J. Si, Z. K. Tan, H. Du, L. Cheng, X. Dai, S. Bai, H. He, Z. Ye, M. L. Lai, R. H. Friend and W. Huang, *Adv. Mater.*, 2015, **27**, 2311–2316.
20 Y. Cheng, X. Guo, Y. Shi and L. Pan, *Nanotechnology*, 2024, **35**, 242001.
21 C. Xie, C.-K. Liu, H.-L. Loi and F. Yan, *Adv. Funct. Mater.*, 2020, **30**, 1903907.
22 J. Zhang, X. G. Hu, K. Ji, S. Zhao, D. Liu, B. Li, P. X. Hou, C. Liu, L. Liu, S. D. Stranks, H. M. Cheng, S. R. P. Silva and W. Zhang, *Nat. Commun.*, 2024, **15**, 2245.
23 X. Li, F. Cao, D. Yu, J. Chen, Z. Sun, Y. Shen, Y. Zhu, L. Wang, Y. Wei, Y. Wu and H. Zeng, *Small*, 2017, **13**, 1603996.
24 Q. Dong, Y. Fang, Y. Shao, P. Mulligan, J. Qiu, L. Cao and J. Huang, *Science*, 2015, **347**, 967–970.
25 K. X. Steirer, P. Schulz, G. Teeter, V. Stevanovic, M. Yang, K. Zhu and J. J. Berry, *ACS Energy Lett.*, 2016, **1**, 360–366.
26 B. Shi, L. Duan, Y. Zhao, J. Luo and X. Zhang, *Adv. Mater.*, 2020, **32**, 1806474.
27 G. Vats, B. Hodges, A. J. Ferguson, L. M. Wheeler and J. L. Blackburn, *Adv. Mater.*, 2023, **35**, e2205459.
28 J. Lee, H. Lee, C. Kim, T. T. T. Nguyen, Y. Kim, G. Jeong, M. Chang, C. Yun and H. Yoon, *J. Phys. Chem. Lett.*, 2023, **14**, 8837–8845.
29 Z. Wang, Y. Yu, W. Wang, X. Li, L. Li, X. Wei, W. Zhou, Y. Huang, J. Lin and H. Liu, *ACS Appl. Nano Mater.*, 2025, **8**, 15140–15149.
30 T. J. Macdonald, M. Batmunkh, C. T. Lin, J. Kim, D. D. Tune, F. Ambroz, X. Li, S. Xu, C. Sol, I. Papakonstantinou, M. A. McLachlan, I. P. Parkin, J. G. Shapter and J. R. Durrant, *Small Methods*, 2019, **3**, 1900164.
31 R. Ihly, A.-M. Dowgiallo, M. Yang, P. Schulz, N. J. Stanton, O. G. Reid, A. J. Ferguson, K. Zhu, J. J. Berry and J. L. Blackburn, *Energy Environ. Sci.*, 2016, **9**, 1439–1449.
32 S. Seo, K. Akino, J. S. Nam, A. Shawky, H. S. Lin, H. Nagaya, E. I. Kauppinen, R. Xiang, Y. Matsuo, I. Jeon and S. Maruyama, *Adv. Mater. Interfaces*, 2022, **9**, 2101595.
33 P. Schulz, A. M. Dowgiallo, M. Yang, K. Zhu, J. L. Blackburn and J. J. Berry, *J. Phys. Chem. Lett.*, 2016, **7**, 418–425.
34 P. Bansal, X. Zhang, H. Wang, P. Kar and W. W. Yu, *Nanoscale Adv.*, 2020, **2**, 808–813.
35 Z. Liu, S. Dai, Y. Wang, B. Yang, D. Hao, D. Liu, Y. Zhao, L. Fang, Q. Ou, S. Jin, J. Zhao and J. Huang, *Adv. Funct. Mater.*, 2020, **30**, 1906335.
36 Z. Dong, W. Li, H. Wang, X. Jiang, H. Liu, L. Zhu and H. Chen, *Matter*, 2022, **5**, 448–481.
37 Q. B. Zhu, B. Li, D. D. Yang, C. Liu, S. Feng, M. L. Chen, Y. Sun, Y. N. Tian, X. Su, X. M. Wang, S. Qiu, Q. W. Li, X. M. Li, H. B. Zeng, H. M. Cheng and D. M. Sun, *Nat. Commun.*, 2021, **12**, 1798.
38 I. Ka, L. F. Gerlein, R. Nechache and S. G. Cloutier, *Sci. Rep.*, 2017, **7**, 45543.
39 C. Perumal Veeramalai, S. Yang, J. Wei, M. Sulaman, R. Zhi, M. I. Saleem, Y. Tang, Y. Jiang and B. Zou, *ACS Appl. Nano Mater.*, 2020, **3**, 459–467.
40 A. A. Marunchenko, M. A. Baranov, E. V. Ushakova, D. R. Ryabov, A. P. Pushkarev, D. S. Gets, A. G. Nasibulin and S. V. Makarov, *Adv. Funct. Mater.*, 2022, **32**, 2109834.
41 H. Zhu, A. Liu, H. L. Luque, H. Sun, D. Ji and Y.-Y. Noh, *ACS Nano*, 2019, **13**, 3971–3981.
42 F. Li, H. Wang, D. Kufer, L. Liang, W. Yu, E. Alarousu, C. Ma, Y. Li, Z. Liu, C. Liu, N. Wei, F. Wang, L. Chen, O. F. Mohammed, A. Fratalocchi, X. Liu, G. Konstantatos and T. Wu, *Adv. Mater.*, 2017, **29**, 1602432.
43 J. Hao, Y. H. Kim, S. N. Habisreutinger, S. P. Harvey, E. M. Miller, S. M. Foradori, M. S. Arnold, Z. Song, Y. Yan, J. M. Luther and J. L. Blackburn, *Sci. Adv.*, 2021, **7**, eabf1959.
44 M. Zhu, H. Yin, J. Cao, L. Xu, P. Lu, Y. Liu, L. Ding, C. Fan, H. Liu, Y. Zhang, Y. Jin, L. M. Peng, C. Jin and Z. Zhang, *Adv. Mater.*, 2024, **36**, 2403743.
45 M. Gao, Y. Park, J. Jin, P.-C. Chen, H. Devyldere, Y. Yang, C. Song, Z. Lin, Q. Zhao, M. Siron, M. C. Scott, D. T. Limmer and P. Yang, *J. Am. Chem. Soc.*, 2023, **145**, 4800–4807.
46 M. Song, B. Zhao, B. Li, K. Wang, Y. Jiang, G. Jia, X. Zhao, B. Yu, Y. Li and F. Yang, *Nat. Synth.*, 2025, **4**, 1056–1067.
47 R. J. Kashtiban, C. E. Patrick, Q. Ramasse, R. I. Walton and J. Sloan, *Adv. Mater.*, 2023, **35**, 2208575.
48 J. Li, P. Dwivedi, K. S. Kumar, T. Roy, K. E. Crawford and J. Thomas, *Adv. Electron. Mater.*, 2021, **7**, 2000535.
49 G. D. Mildred, S. Dresselhaus and P. Avouris, *Carbon Nanotubes: Synthesis, Structure, Properties and Applications*, Springer Berlin, Heidelberg, 1st edn, 2001.
50 B. M. Wieliczka, S. N. Habisreutinger, K. Schutt, J. L. Blackburn and J. M. Luther, *Adv. Energy Mater.*, 2023, **13**, 2204351.
51 M. Kędziora, A. Opala, R. Mastria, L. De Marco, M. Król, K. Łempicka-Mirek, K. Tyszka, M. Ekielski, M. Guziewicz, K. Bogdanowicz, A. Szerling, H. Sigurðsson, T. Czyszanowski, J. Szczytko, M. Matuszewski, D. Sanvitto and B. Piętka, *Nat. Mater.*, 2024, **23**, 1515–1522.
52 J. Zheng, C. Luo, B. Shabbir, C. Wang, W. Mao, Y. Zhang, Y. Huang, Y. Dong, J. J. Jasieniak, C. Pan and Q. Bao, *Nanoscale*, 2019, **11**, 8020–8026.
53 B. Pradhan, S. Das, J. Li, F. Chowdhury, J. Cherusseri, D. Pandey, D. Dev, A. Krishnaprasad, E. Barrios, A. Towers, A. Gesquiere, L. Tetard, T. Roy and J. Thomas, *Sci. Adv.*, 2020, **6**, eaay5225.
54 W. Xu, Y. Guo, X. Zhang, L. Zheng, T. Zhu, D. Zhao, W. Hu and X. Gong, *Adv. Funct. Mater.*, 2018, **28**, 1705541.
55 P. Luo, Y. Zhou, S. Zhou, Y. Lu, C. Xu, W. Xia and L. Sun, *Chem. Eng. J.*, 2018, **343**, 146–154.
56 Z. Chen, L. Dong, H. Tang, Y. Yu, L. Ye and J. Zang, *CrystEngComm*, 2019, **21**, 1389–1396.

57 Note: Although XRD samples were prepared in a controlled environment, they often degrade during transfer to the XRD instrument due to the high sensitivity of Cs-based perovskites.
58 S. M. Bachilo, M. S. Strano, C. Kittrell, R. H. Hauge, R. E. Smalley and R. B. Weisman, *Science*, 2002, **298**, 2361–2366.
59 K. Cui, Y. Qian, I. Jeon, A. Anisimov, Y. Matsuo, E. I. Kauppinen and S. Maruyama, *Adv. Energy Mater.*, 2017, **7**, 1700449.
60 I. O. Maciel, N. Anderson, M. A. Pimenta, A. Hartschuh, H. Qian, M. Terrones, H. Terrones, J. Campos-Delgado, A. M. Rao, L. Novotny and A. Jorio, *Nat. Mater.*, 2008, **7**, 878–883.
61 M. S. Dresselhaus, A. Jorio, M. Hofmann, G. Dresselhaus and R. Saito, *Nano Lett.*, 2010, **10**, 751–758.
62 Z. Li, S. A. Kulkarni, P. P. Boix, E. Shi, A. Cao, K. Fu, S. K. Batabyal, J. Zhang, Q. Xiong, L. H. Wong, N. Mathews and S. G. Mhaisalkar, *ACS Nano*, 2014, **8**, 6797–6804.
63 J. Zhang, C. Wang, H. Fu, L. Gong, H. He, Z. Fang, C. Zhou, J. Chen, Z. Chao and J. Fan, *J. Alloys Compd.*, 2021, **862**, 158454.
64 P. Fooladvand, M. Eskandari, D. Fathi and N. Das, *Energy Rep.*, 2023, **10**, 3652–3664.
65 T. A. Shastry, P. E. Hartnett, M. R. Wasielewski, T. J. Marks and M. C. Hersam, *ACS Energy Lett.*, 2016, **1**, 548–555.
66 L. Du, W. Xiong, W. K. Chan and D. L. Phillips, *Nanophotonics*, 2020, **9**, 4689–4701.
67 B. Liu, F. Wu, H. Gui, M. Zheng and C. Zhou, *ACS Nano*, 2017, **11**, 31–53.
68 W. A. Gaviria Rojas and M. C. Hersam, *Adv. Mater.*, 2020, **32**, 1905654.
69 S. Ghasemi and K. Moth-Poulsen, *Nanoscale*, 2021, **13**, 659–671.
70 A. D. Franklin, M. C. Hersam and H. S. P. Wong, *Science*, 2022, **378**, 726–732.
71 H. Lu, W. Wu, Z. He, X. Han and C. Pan, *Nanoscale Horiz.*, 2023, **8**, 1014–1033.